

Nonlinear radiation phenomena for Casson–Maxwell nanoliquid flow with chemical reactions

Kotha Gangadhar¹ , Eathakoti Mary Victoria²,
Konduru Bhanu Lakshmi³  and Ali J Chamkha⁴

Proc IMechE Part E:
J Process Mechanical Engineering

1–11

© IMechE 2022

Article reuse guidelines:

sagepub.com/journals-permissions

DOI: 10.1177/09544089221132356

journals.sagepub.com/home/pie



Abstract

The viscoelastic characteristics of an incompressible, axisymmetric Casson–Maxwell nanoliquid flow between two stationary discs were examined in this paper. Two porous discs are constrained for uniform injection. The Christov model is used in conjunction with the Buongiorno model. In an energy equation with a nonlinear form, thermal radiation characteristics are used. In the current continuation, the impact of chemical reactions is taken into account, making the work more adaptable. Using appropriate transformations, the constructed model was transformed into a dimensionless form. The solution is obtained by employing the FEM technique. The related parameters are described using physical results. The radial velocity distribution at the center line was reduced using a magnetic parameter and a Casson parameter. When the Brownian motion constant and radiation parameter are increased, the temperature distribution of nanoparticles enhances. Furthermore, the rate of the reaction increases in the presence of a chemical reaction. Pearson's correlation coefficient was used to discover a relationship between the Sherwood and Nusslet numbers. To determine the linear relationship between variables, the *t*-test method is used.

Keywords

Porous disc, Casson–Maxwell fluid, nonlinear thermal radiation, Buongiorno theory, finite element method, chemical reaction

Date received: 26 May 2022; accepted: 20 September 2022

Introduction

The Casson model is one of the most fundamental forms of non-Newtonian liquid construction. It controls the viscoelasticity of different fluid flows. As a result, it begins to deform like a soft solid when yield stress exceeds shear stress. Shear stress is infinite. Mahanthesh et al.¹ invented the exponential space-dependent heat source and the cross-diffusion effect in convective heat and mass transfer as a result of the infinite disc. Shehzad et al.² imposed the Maxwell liquid flow using the Christov theory and thermophoresis. They explained that as the Deborah number increases, the velocity field decays. Mushtaq et al.³ investigate the viscoelastic properties of an incompressible axisymmetric Casson liquid flow between two discs. Nazir et al.⁴ investigated the dynamics of Casson liquid flow over a time-dependent stretchable sheet subjected to a magnetic field. They invented that magnetic field is the reason for hindrance to flow. Under the influence of melting heat transport flow of nonlinear liquid over a Riga plate stated by Obalalu et al.,⁵ Lanjwani et al.⁶ investigated radiated flat plate magnetized boundary layer Fe-Casson fluid. Givi and Sangeetha George⁷ investigated the unstable free convection slip flow of Casson liquid across a vertical permeable plate. Mahmud et al.⁸ studied the stagnation point stream of hydrodynamic shear-thinning

nanofluid. Nandeppanavar et al.⁹ studied the mass and heat transport of convection Casson liquid flow across a moving vertical plate using nonlinear thermal radiation. Das et al.¹⁰ investigated an infinite vertical plate boundary layer flow of an electrically conducting Casson fluid with mass and heat transport. They also investigated the infinite vertical plate boundary layer flow with mass and heat transport of an electrically conducting Casson liquid. Gangadhar et al.¹¹ investigated entropy minimization in Casson liquid boundary layer flow in the presence of a magnetic field.

The flow of electrically conducting liquid is the primary cause of variation in magnetic lines and flux.

¹Department of Mathematics, Acharya Nagarjuna University Campus, Ongole, Andhra Pradesh, India

²Department of Mathematics, Swarnandhra Institute of Engineering and Technology, Narasapuram, Andhra Pradesh, India

³Department of Mathematics, Lakireddy Bali Reddy College of Engineering, Mylavaram, Andhra Pradesh, India

⁴Faculty of Engineering, Kuwait College of Science and Technology, Doha, Kuwait

Corresponding author:

Kotha Gangadhar, Department of Mathematics, Acharya Nagarjuna University Campus, Ongole, Andhra Pradesh 523001, India.

Email: kgangadharmaths@gmail.com

As a result, the fluid experienced a Lorentz force. This is known as magnetohydrodynamic (MHD) flow. Several authors have investigated these flows. Saleem et al.¹² investigated the effects of viscous dispersion and heat suction/injection on heat transport features in nanomaterials at the same time. Wehgal and Ashraf¹³ investigated an electrically conducting liquid's MHD axisymmetric stream between two infinite equivalent stationary coaxial porous discs. Turkyilmazoglu¹⁴ investigated the liquid flow and heat transport between two stretchable discs. Ashraf and Wehgal¹⁵ created a model that depicted the axisymmetric laminar flow of an electrically conducting micropolar liquid between two infinite parallel discs. Reddy et al.¹⁶ presented a numerical simulation of a MHD liquid flow along with a non-isothermal stretched sheet using the Soret and Dufour equations. Mahabaleshwar et al.¹⁷ investigated an inclined MHD micropolar fluid flow caused by surface stretching/shrinking in the presence of mass transpiration and thermal radiation. Jamshed et al.¹⁸ investigated heat transmission and steady MHD mixed convection flow in vented porous enclosing spaces using a heated elliptic inner cylinder filled with nanofluid. In a laboratory-scale system, Blishchik et al.¹⁹ investigated the continuous coating of turbulent liquid metal flow numerical solutions. Giresha et al.²⁰ investigated Carreau liquid flow heat transfer on a porous sensor plane. Ahmad et al.²¹ investigated three-dimensional MHD Maxwell liquid flow along with a Joule heated surface. Narasimha Rao and Gangadhar²² investigated the unsteady 3D boundary layer flow with viscous dissipation.

Heat transfer is a fascinating method in technology and industry. Fourier²³ proposed the first model for describing heat transport. The calculation of this model yields a parabolic energy equation. Cattaneo²⁴ used relaxation time formulas to simplify this model, resulting in the hyperbolic form of the energy equation. This add-on allows for heat transpiration via thermal waves that travel at a constant speed. Christov²⁵ added another useful modification by replacing the time derivative with the upper convected derivative of the Oldroyd-B equation. After this fascinating adjustment, many authors used this formula to report the heat transport characteristics in many fluid phenomena. Hashim and Khan,²⁶ for example, simulated the Cattaneo–Christov heat flux laws for Carreau fluid flow over the slandering surface. The impact of entropy generation on the unsteady flow of Oldroyd-B nanofluid was studied by Bai et al.²⁷ using a wedge implanted in porous media. Ali et al.²⁸ looked at the generalized Fourier's heat flux and homogeneous–heterogeneous reactions in a three-dimensional non-Newtonian cross fluid flow. Venkata Ramana et al.²⁹ investigated the Oldroyd-B fluid in MHD flow with Cattaneo–Christov heat flux on a nonlinear stretched sheet of varying thickness.

During the last few years, nanotechnology has gained significant attention from researchers. Nanomaterials are made by dispersing small-scale solid nanoparticles, which have better thermal efficiency than standard fluids. Air, water, ethylene glycol and oil are examples of low thermal conductivity fluids. The use of nanoparticles

to improve the heat transport properties of classical fluids has proven to be effective. These nanoparticles have physical and chemical properties similar to regular liquids but with higher thermal conductivity. Nanomaterials serve a critical function in boosting cooling rates and thermal capacity. Nanomaterials are used in electronic cooling, heat exchangers, microelectronics cooling, automotive cooling, vehicle thermal management and cancer therapy. The term “nanofluid” was first created by Choi and Eastman³⁰ to describe how the dispersion of metallic nanoparticles in regular liquids can significantly increase thermal efficiency. Following Choi's research, Buongiorno³¹ created a model to show how thermal conduction enhancement occurs in nanomaterials. He investigated seven different slip processes and discovered that only thermophoretic and Brownian diffusion properties count for increased heat transport. The flow of the nanomaterial Cu-H₂O through an enclosure was studied by Abu-Nada and Oztop.³² López et al.³³ calculated heat transfer and entropy generation in a porous vertical microchannel with an Al₂O₃–water nanofluid MHD flow. Kumar et al.³⁴ used von Karman's radiative hydro-magnetic nanofluid flow between two coaxial rotating porous discs to generate entropy. On a linear permeable stretched surface, Gangadhar et al.^{36–41} explored the formation of entropy and the application of an angled magnetic field to Williamson nanoliquid. Recent research on the flow of nanofluids with different flow characteristics may be found in.^{36–41}

The nonlinear Casson–Maxwell liquid between two porous discs using the Buongiorno theory, using extra impacts of nonlinear heat transfer and chemical reactions, has yet to be researched, according to the literature review. The essential transformations are used to convert nonlinear coupled expressions to ordinary differentials. To display numerical solutions using the finite element method (FEM), a computer methodology has been developed.^{4,18,34} The mass and heat transfer rates were examined using tabled values. The strength of the linear relationship between the Sherwood and Nusselt numbers is evaluated using Pearson's coefficient correlation method,³⁶ and the statistical significance of the linear relationship is established using the *t*-test method.

Flow formation

Consider the flow of an axisymmetric, incompressible Casson fluid between two stationary discs. The Cattaneo–Christov theory is applied in the flow model. The energy equation takes into consideration nonlinear thermal radiation because a fluid heats up when current flows through it. Chemical reactions are used to alter the associated expression for concentration profiles. The lower disc is at $z_0 = -a_0$, while the upper disc is at $z_0 = a_0$. Magnetic field B_0 applied to stationary discs in the axial direction. The flow is subjected to a uniform magnetic field that is applied vertically, and the induced field is ignored. Assume there is no polarization voltage. Consider the cylinder coordinate system (r_0, θ_0, z_0) . Because of the flow assumption, calculations

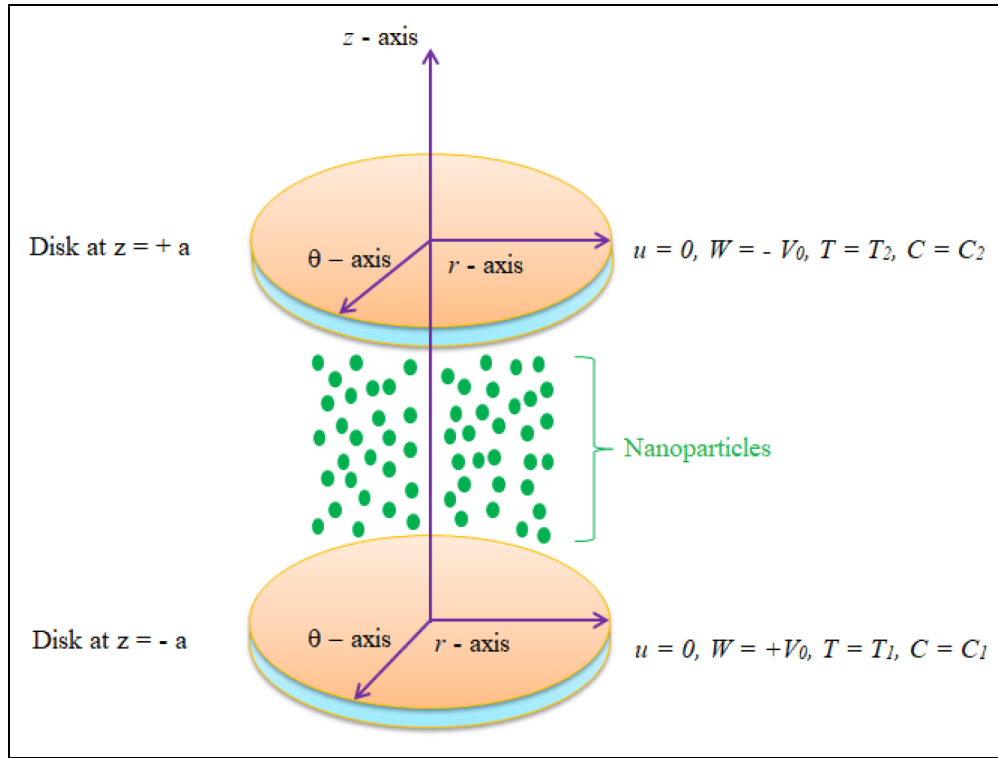


Figure 1. Physical flow configuration.

in the θ -direction are omitted. Lower and upper disc temperatures are represented by T_1 & T_2 . Similarly, concentrations are C_1 & C_2 . The physical model is given in Figure 1.

The following are the governing equations:

$$\frac{\partial \hat{u}_0}{\partial \hat{r}_0} + \frac{\hat{u}_0}{\hat{r}_0} + \frac{\partial \hat{w}_0}{\partial \hat{z}_0} = 0, \quad (1)$$

$$\begin{aligned} \hat{u}_0 \frac{\partial \hat{u}_0}{\partial \hat{r}_0} + \hat{w}_0 \frac{\partial \hat{u}_0}{\partial \hat{z}_0} &= -\frac{1}{\rho} \frac{\partial p}{\partial \hat{r}_0} + \nu \left(1 + \frac{1}{\beta}\right) \\ &\left[2 \frac{\partial^2 \hat{u}_0}{\partial \hat{r}_0^2} + \frac{\partial^2 \hat{u}_0}{\partial \hat{z}_0^2} + \frac{\partial^2 \hat{w}_0}{\partial \hat{r}_0 \partial \hat{z}_0} + \frac{2}{\hat{r}_0} \frac{\partial \hat{u}_0}{\partial \hat{r}_0} - 2 \frac{\hat{u}_0}{\hat{r}_0^2} \right] \\ &- \gamma_1 \left(\hat{u}_0^2 \frac{\partial^2 \hat{u}_0}{\partial \hat{r}_0^2} + \hat{w}_0^2 \frac{\partial^2 \hat{u}_0}{\partial \hat{z}_0^2} + 2 \hat{u}_0 \hat{w}_0 \frac{\partial^2 \hat{u}_0}{\partial \hat{r}_0 \partial \hat{z}_0} \right) \\ &- \frac{\sigma_e B_0^2}{\rho} \left(\hat{u}_0 + \hat{w}_0 \gamma_0 \frac{\partial \hat{u}_0}{\partial \hat{z}_0} \right), \quad (2) \end{aligned}$$

$$\begin{aligned} \hat{u}_0 \frac{\partial \hat{w}_0}{\partial \hat{r}_0} + \hat{w}_0 \frac{\partial \hat{w}_0}{\partial \hat{z}_0} &= -\frac{1}{\rho} \frac{\partial p}{\partial \hat{z}_0} \\ &+ \nu \left(1 + \frac{1}{\beta}\right) \left[\frac{\partial^2 \hat{u}_0}{\partial \hat{r}_0 \partial \hat{z}_0} + \frac{\partial^2 \hat{w}_0}{\partial \hat{r}_0^2} + \frac{1}{\hat{r}_0} \frac{\partial \hat{u}_0}{\partial \hat{z}_0} + \frac{1}{\hat{r}_0} \frac{\partial \hat{w}_0}{\partial \hat{r}_0} + 2 \frac{\partial^2 \hat{w}_0}{\partial \hat{z}_0^2} \right] \\ &- \gamma_0 \left(\hat{u}_0^2 \frac{\partial^2 \hat{w}_0}{\partial \hat{r}_0^2} + \hat{w}_0^2 \frac{\partial^2 \hat{w}_0}{\partial \hat{z}_0^2} + 2 \hat{u}_0 \hat{w}_0 \frac{\partial^2 \hat{w}_0}{\partial \hat{r}_0 \partial \hat{z}_0} \right), \quad (3) \end{aligned}$$

$$\begin{aligned} \rho c_p \left(\hat{u}_0 \frac{\partial T_0}{\partial \hat{r}_0} + \hat{w}_0 \frac{\partial T_0}{\partial \hat{z}_0} \right) &= k_0 \left(\frac{\partial^2 T_0}{\partial \hat{r}_0^2} + \frac{1}{\hat{r}_0} \frac{\partial T_0}{\partial \hat{r}_0} + \frac{\partial^2 T_0}{\partial \hat{z}_0^2} \right) \\ &+ \tau \left[D_B \left(\frac{\partial T_0}{\partial \hat{r}_0} \frac{\partial C_0}{\partial \hat{r}_0} + \frac{\partial T_0}{\partial \hat{z}_0} \frac{\partial C_0}{\partial \hat{z}_0} \right) + \frac{D_T}{T_m} \left(\left(\frac{\partial T_0}{\partial \hat{r}_0} \right)^2 + \left(\frac{\partial T_0}{\partial \hat{z}_0} \right)^2 \right) \right] \\ &- \gamma_1 \left\{ \hat{u}_0^2 \frac{\partial^2 T_0}{\partial \hat{r}_0^2} + \hat{w}_0^2 \frac{\partial^2 T_0}{\partial \hat{z}_0^2} + 2 \hat{u}_0 \hat{w}_0 \frac{\partial^2 T_0}{\partial \hat{r}_0 \partial \hat{z}_0} \right. \\ &\left. + \left(\hat{u}_0 \frac{\partial \hat{u}_0}{\partial \hat{r}_0} + \hat{w}_0 \frac{\partial \hat{u}_0}{\partial \hat{z}_0} \right) \frac{\partial T_0}{\partial \hat{r}_0} + \left(\hat{u}_0 \frac{\partial \hat{w}_0}{\partial \hat{r}_0} + \hat{w}_0 \frac{\partial \hat{w}_0}{\partial \hat{z}_0} \right) \frac{\partial T_0}{\partial \hat{z}_0} \right\} \\ &- \frac{\partial \hat{q}_r}{\partial \hat{r}_0}, \quad (4) \end{aligned}$$

$$\begin{aligned} \hat{u}_0 \frac{\partial C_0}{\partial \hat{r}_0} + \hat{w}_0 \frac{\partial C_0}{\partial \hat{z}_0} &= D_B \left(\frac{\partial^2 C_0}{\partial \hat{r}_0^2} + \frac{1}{\hat{r}_0} \frac{\partial C_0}{\partial \hat{r}_0} + \frac{\partial^2 C_0}{\partial \hat{z}_0^2} \right) \\ &+ \frac{D_T}{T_m} \left(\frac{\partial^2 T_0}{\partial \hat{r}_0^2} + \frac{1}{\hat{r}_0} \frac{\partial T_0}{\partial \hat{r}_0} + \frac{\partial^2 T_0}{\partial \hat{z}_0^2} \right) - k_1 (C_0 - C_1). \quad (5) \end{aligned}$$

Specifies the boundary conditions at the two discs are¹⁵:

$$\begin{cases} \hat{u}_0 = 0, \hat{w}_0 = +V_0, T_0 = T_1, C_0 = C_1 & \text{at } \hat{z}_0 = -a_0, \\ \hat{u}_0 = 0, \hat{w}_0 = -V_0, T_0 = T_2, C_0 = C_2 & \text{at } \hat{z}_0 = +a_0. \end{cases} \quad (6)$$

Here, T_0 is the temperature, B_0 is the magnetic field strength, β is the Casson parameter, c_p is the specific heat, σ_e is the electrical conductivity, ν is the kinematic viscosity, k_1 is the chemical reaction rate constant, p is

the pressure, C_0 is the concentration, γ_0 is the relaxation time parameter, γ_1 is the thermal relaxation time, τ is the nanoparticle ratio of base fluid capacity and heat, D_B is the Brownian diffusion, T_m is the mean liquid temperature, D_T is the thermophoretic diffusion coefficient, and V_0 is the injection velocity.

According to the Rosseland approximation, \hat{q}_r can be written as³³:

$$\hat{q}_r = -\frac{4\sigma_s}{3k^*} \frac{\partial T_0^4}{\partial \hat{r}_0} = -\frac{16\sigma_s}{3k^*} T_0^3 \frac{\partial T_0}{\partial \hat{r}_0}, \quad (7)$$

where σ^* represents mean absorptions coefficient and k^* is the Boltzmann constant.

Following similarity transformations applied to calculate the temperature, concentration distribution and velocity:

$$\begin{aligned} \hat{u}_0 &= \frac{\hat{r}_0 V_0}{2a_0} \tilde{f}'_1(\tilde{\eta}), \quad \hat{w}_0 = -V_0 \tilde{f}_1(\tilde{\eta}), \\ \tilde{\eta} &= \frac{\hat{z}_0}{a_0}, \quad \tilde{\theta}_1 = \frac{T_0 - T_2}{T_1 - T_2}, \quad \tilde{\phi}_1 = \frac{C_0 - C_2}{C_1 - C_2}. \end{aligned} \quad (8)$$

The similarity function in equation (8) satisfies equation (1). By eliminating the pressure term, equations (2) to (5) are written as

$$\begin{aligned} \left(1 + \frac{1}{\beta}\right) \tilde{f}_1'''' + DeRe(\tilde{f}_1 \tilde{f}_1''^2 + \tilde{f}_1'^2 \tilde{f}_1'' - \tilde{f}_1^2 \tilde{f}_1'''' - \tilde{f}_1 \tilde{f}_1' \tilde{f}_1''''') \\ + Re \tilde{f}_1 \tilde{f}_1'''' - M^2 Re(\tilde{f}_1'' - De(\tilde{f}_1' \tilde{f}_1'' + \tilde{f}_1 \tilde{f}_1''')) = 0, \end{aligned} \quad (9)$$

$$\begin{aligned} \left[1 + \frac{4}{3} Rd(1 + (\theta_w - 1)\tilde{\theta}_1)^3\right] \theta_1'' \\ + Rd[3(\theta_w - 1)\tilde{\theta}_1^2][1 + (\theta_w - 1)\tilde{\theta}_1]^2 \\ + Pr Re \tilde{f}_1 \tilde{\theta}_1' + Pr Nt \tilde{\theta}_1'^2 + Pr Nb \tilde{\theta}_1' \tilde{\phi}_1' \\ - Pr \lambda_1 Re(\tilde{f}_1 \tilde{f}_1' \tilde{\theta}_1' + \tilde{f}_1^2 \tilde{\theta}_1'') = 0, \end{aligned} \quad (10)$$

$$\tilde{\phi}_1'' + \left(\frac{Nt}{Nb}\right) \tilde{\theta}_1'' + Re Pr Le \tilde{f}_1 \tilde{\phi}_1' - Pr Le \gamma \tilde{\phi}_1 = 0. \quad (11)$$

By using equation (8), the boundary conditions are changed to the following forms:

$$\begin{cases} \tilde{f}_1'(-1) = 0, \tilde{f}_1(-1) = -1, \tilde{\theta}_1(-1) = 1, \tilde{\phi}_1(-1) = 1, \\ \tilde{f}_1'(1) = 0, \tilde{f}_1(1) = 1, \tilde{\theta}_1(1) = 0, \tilde{\phi}_1(1) = 0. \end{cases} \quad (12)$$

In the above equations,

Here, De is Deborah number, Nb is Brownian movement parameter, M is magnetic parameter, Nt is thermophoretic parameter, Re is Reynolds number, Rd is radiation factor, Le is Lewis number, θ_w is temperature ratio parameter, γ is chemical reaction parameter, γ_1 is thermal relaxation time factor, and Pr is Prandtl number.

Turkyilmazoglu¹⁴ determines the Sherwood and local Nusselt numbers at both discs:

$$\begin{aligned} Nu_{-1r} &= -\theta_1'(-1), \quad Nu_{+1r} = -\theta_1'(1), \quad Sh_{-1r} \\ &= -\phi_1'(-1), \quad Sh_{+1r} = -\phi_1'(1). \end{aligned} \quad (13)$$

Finite element formulation

If $\tilde{f}_1 = p$ and $p' = q$, then the weighted integral form of the residuals for coupled nonlinear boundary value problem (equations 9–11) over the typical element $(\tilde{\eta}_b, \tilde{\eta}_{b+1})$ is

$$\int_{\tilde{\eta}_b}^{\tilde{\eta}_{b+1}} w_1 [\tilde{f}_1 - p] d\tilde{\eta} = 0, \quad (14)$$

$$\int_{\tilde{\eta}_b}^{\tilde{\eta}_{b+1}} w_2 [p' - q] d\tilde{\eta} = 0, \quad (15)$$

$$\begin{aligned} \int_{\tilde{\eta}_b}^{\tilde{\eta}_{b+1}} w_3 \left[\left(1 + \frac{1}{\beta}\right) q'' + DeRe(\tilde{f}_1 q^2 + p^2 q - \tilde{f}_1^2 q' - \tilde{f}_1 p q') \right. \\ \left. + Re \tilde{f}_1 q' - M^2 Re(q - De(pq + \tilde{f}_1 q')) \right] d\tilde{\eta} \\ = 0, \end{aligned} \quad (16)$$

$$\int_{\tilde{\eta}_b}^{\tilde{\eta}_{b+1}} w_4 \left[\left[1 + \frac{4}{3} Rd(1 + (\theta_w - 1)\tilde{\theta}_1)^3\right] \theta_1'' \right. \\ \left. + Rd[3(\theta_w - 1)\tilde{\theta}_1^2][1 + (\theta_w - 1)\tilde{\theta}_1]^2 \right. \\ \left. + Pr Re \tilde{f}_1 \tilde{\theta}_1' + Pr Nt \tilde{\theta}_1'^2 + Pr Nb \tilde{\theta}_1' \tilde{\phi}_1' \right. \\ \left. - Pr \lambda_1 Re(\tilde{f}_1 p \tilde{\theta}_1' + \tilde{f}_1^2 \tilde{\theta}_1'') \right] d\tilde{\eta} = 0, \quad (17)$$

$$\int_{\tilde{\eta}_b}^{\tilde{\eta}_{b+1}} w_5 \left[\tilde{\phi}_1'' + \left(\frac{Nt}{Nb}\right) \tilde{\theta}_1'' + Re Pr Le \tilde{f}_1 \tilde{\phi}_1' - Pr Le \gamma \tilde{\phi}_1 \right] d\tilde{\eta} \\ = 0, \quad (18)$$

where arbitrary functions are w_1, w_2, w_3, w_4 , and w_5 . By putting the following finite element approximation form

$$\begin{cases} De = \gamma_0 V_0, \quad M = \sqrt{\frac{\sigma_e a_0 B_0^2}{\rho V_0}}, \quad Pr = \frac{\mu c_p}{\rho k_0}, \quad Re = \frac{\rho V_0 a_0}{\mu}, \quad Rd = \frac{4\sigma_s T_\infty^3}{kk^*}, \quad \theta_w = \frac{T_1}{T_2}, \\ Nb = \frac{\tau D_T}{v T_m} (T_1 - T_2), \quad Nt = \frac{\tau D_B}{v} (C_1 - C_2), \quad \lambda_1 = \frac{\gamma_1 V_0}{a_0}, \quad Le = \frac{\alpha}{D_B}, \quad \gamma = \frac{k_1}{V_0}, \end{cases}$$

into equations (14) to (18), the finite element model can be obtained:

$$\begin{aligned} f &= \sum_{n=1}^3 f_n \Omega_n, p = \sum_{n=1}^3 p_n \Omega_n, \\ q &= \sum_{n=1}^3 q_n \Omega_n, \theta = \sum_{n=1}^3 \theta_n \Omega_n, \\ \phi &= \sum_{n=1}^3 \phi_n \Omega_n, \end{aligned} \quad (19)$$

With $w_1 = w_2 = w_3 = w_4 = w_5 = \Omega_n$ ($n = 1, 2, 3$), here test functions Ω_n for a characteristic length element $(\tilde{\eta}_b, \tilde{\eta}_{b+1})$ are as follows:

$$\begin{aligned} \Omega_1 &= \frac{(\tilde{\eta}_{b+1} - \tilde{\eta}_b - 2\tilde{\eta})(\tilde{\eta}_{b+1} - \tilde{\eta})}{(\tilde{\eta}_{b+1} - \tilde{\eta}_b)^2}, \\ \Omega_2 &= \frac{4(\tilde{\eta} - \tilde{\eta}_b)(\tilde{\eta}_{b+1} - \tilde{\eta})}{(\tilde{\eta}_{b+1} - \tilde{\eta}_b)^2}, \\ \Omega_3 &= \frac{(\tilde{\eta}_{b+1} - \tilde{\eta}_b - 2\tilde{\eta})(\tilde{\eta} - \tilde{\eta}_{b+1})}{(\tilde{\eta}_{b+1} - \tilde{\eta}_b)^2}, \\ \tilde{\eta}_b &\leq \tilde{\eta} \leq \tilde{\eta}_{b+1}. \end{aligned} \quad (20)$$

The following is the model of finite elements of the equations and hence developed:

$$\begin{bmatrix} [\Pi^{11}] & [\Pi^{12}] & [\Pi^{13}] & [\Pi^{14}] & [\Pi^{15}] \\ [\Pi^{21}] & [\Pi^{22}] & [\Pi^{23}] & [\Pi^{24}] & [\Pi^{25}] \\ [\Pi^{31}] & [\Pi^{32}] & [\Pi^{33}] & [\Pi^{34}] & [\Pi^{35}] \\ [\Pi^{41}] & [\Pi^{42}] & [\Pi^{43}] & [\Pi^{44}] & [\Pi^{45}] \\ [\Pi^{51}] & [\Pi^{52}] & [\Pi^{53}] & [\Pi^{54}] & [\Pi^{55}] \end{bmatrix} \begin{bmatrix} \{f\} \\ \{p\} \\ \{q\} \\ \{\theta\} \\ \{\phi\} \end{bmatrix} = \begin{bmatrix} \{b_1\} \\ \{b_2\} \\ \{b_3\} \\ \{b_4\} \\ \{b_5\} \end{bmatrix} \quad (21)$$

where $[\Pi^{mm}]$ and $[b_m]$ ($m, n = 1, 2, 3, 4, 5$) are defined as:

$$\begin{aligned} \Pi_{ij}^{11} &= \int_{\tilde{\eta}_b}^{\tilde{\eta}_{b+1}} \Omega_i \frac{d\Omega_j}{d\tilde{\eta}} d\tilde{\eta}, \Pi_{ij}^{12} = - \int_{\tilde{\eta}_b}^{\tilde{\eta}_{b+1}} \Omega_i \Omega_j d\tilde{\eta}, \Pi_{ij}^{13} = \Pi_{ij}^{14} \\ &= \Pi_{ij}^{15} = 0, \\ \Pi_{ij}^{22} &= \int_{\tilde{\eta}_b}^{\tilde{\eta}_{b+1}} \Omega_i \frac{d\Omega_j}{d\tilde{\eta}} d\tilde{\eta}, \Pi_{ij}^{23} = - \int_{\tilde{\eta}_b}^{\tilde{\eta}_{b+1}} \Omega_i \Omega_j d\tilde{\eta}, \Pi_{ij}^{21} = \Pi_{ij}^{24} \\ &= \Pi_{ij}^{25} = 0, \end{aligned}$$

$$\Pi_{ij}^{33} = \int_{\tilde{\eta}_b}^{\tilde{\eta}_{b+1}} \begin{bmatrix} - \left(1 + \frac{1}{\beta} - \text{ReDe} \bar{f}_1^2\right) \frac{d\Omega_i d\Omega_j}{d\tilde{\eta} d\tilde{\eta}} \\ + \text{DeRe} \bar{q} \Omega_i \Omega_j \\ - \text{DeRe} \bar{f}_1 \Omega_i \frac{d\Omega_j}{d\tilde{\eta}} \\ + \text{Re} \Omega_i \frac{d\Omega_j}{d\tilde{\eta}} - M^2 \text{Re} \Omega_i + M^2 \text{ReDe} \Omega_i \Omega_j \\ + M^2 \text{DeRe} \Omega_i \frac{d\Omega_j}{d\tilde{\eta}} \end{bmatrix} d\tilde{\eta},$$

$$\begin{aligned} \Pi_{ij}^{32} &= \int_{\tilde{\eta}_b}^{\tilde{\eta}_{b+1}} \text{DeRe} \bar{p} \Omega_i \Omega_j d\tilde{\eta}, \Pi_{ij}^{31} = \Pi_{ij}^{34} = \Pi_{ij}^{35} = 0, \Pi_{ij}^{44} \\ &= \int_{\tilde{\eta}_b}^{\tilde{\eta}_{b+1}} \begin{bmatrix} - \left(1 + \frac{4}{3} \text{Rd}(1 + (\theta_w - 1)\bar{\theta}_1)^3 - \text{Pr} \lambda_1 \text{Re} \bar{f}_1^2\right) \\ \frac{d\Omega_i d\Omega_j}{d\tilde{\eta} d\tilde{\eta}} + 3 \text{Rd}(\theta_w - 1) \bar{\theta}'_1 \Omega_i \frac{d\Omega_j}{d\tilde{\eta}} \\ + 3 \text{Rd}(\theta_w - 1)^3 \bar{\theta}'_1 \bar{\theta}_1^2 \Omega_i \frac{d\Omega_j}{d\tilde{\eta}} \\ + 6 \text{Rd}(\theta_w - 1)^2 \bar{\theta}'_1{}^2 \Omega_i \Omega_j + \text{Pr} \text{Re} \bar{f}_1 \Omega_i \frac{d\Omega_j}{d\tilde{\eta}} \\ + \text{Pr} \text{Ni} \bar{\theta}'_1 \Omega_i \frac{d\Omega_j}{d\tilde{\eta}} + \text{Pr} \text{Nb} \bar{\phi}'_1 \Omega_i \frac{d\Omega_j}{d\tilde{\eta}} \\ + \text{Pr} \lambda_1 \text{Re} \bar{f}_1 \bar{p} \Omega_i \frac{d\Omega_j}{d\tilde{\eta}} \end{bmatrix} d\tilde{\eta}, \Pi_{ij}^{41} \\ &= \Pi_{ij}^{42} = \Pi_{ij}^{43} = \Pi_{ij}^{45} = 0, \Pi_{ij}^{55} \\ &= \int_{\tilde{\eta}_b}^{\tilde{\eta}_{b+1}} \left[- \frac{d\Omega_i d\Omega_j}{d\tilde{\eta} d\tilde{\eta}} + \text{Pr} \text{LeRe} \bar{f}_1 \Omega_i \frac{d\Omega_j}{d\tilde{\eta}} - \text{Pr} \text{Le} \gamma \Omega_i \Omega_j \right] d\tilde{\eta}, \Pi_{ij}^{51} \\ &= \Pi_{ij}^{52} = \Pi_{ij}^{53} = \Pi_{ij}^{54} = 0, \end{aligned}$$

And

$$\begin{aligned} b_i^1 &= 0, b_i^2 = 0, b_i^3 = - \left[1 + \frac{1}{\beta} - \text{ReDe} \bar{f}_1^2 \right] \left(\Omega_i \frac{dq}{d\tilde{\eta}} \right)_{\tilde{\eta}_b}^{\tilde{\eta}_{b+1}}, \\ b_i^4 &= - \left(1 + \frac{4}{3} \text{Rd}(1 + (\theta_w - 1)\bar{\theta}_1)^3 - \text{Pr} \lambda_1 \text{Re} \bar{f}_1^2 \right) \\ &\left(\Omega_i \frac{d\theta_1}{d\tilde{\eta}} \right)_{\tilde{\eta}_b}^{\tilde{\eta}_{b+1}}, b_i^5 = - \left(\Omega_i \frac{d\phi_1}{d\tilde{\eta}} \right)_{\tilde{\eta}_b}^{\tilde{\eta}_{b+1}} \end{aligned}$$

With

$$\begin{aligned} \bar{f}_1 &= \sum_{n=1}^3 \bar{f}_n \Omega_n, \bar{p} = \sum_{n=1}^3 \bar{p}_n \Omega_n, \bar{q} = \sum_{n=1}^3 \bar{q}_n \Omega_n, \bar{\theta}'_1 \\ &= \sum_{n=1}^3 \bar{\theta}'_n \Omega_n, \bar{\phi}'_1 = \sum_{n=1}^3 \bar{\phi}'_n \Omega_n. \end{aligned}$$

Before we can explain the graphical analysis for the desired parameters, we must validate our numerical solution. Table 1 was created to verify our numerical approach, with $Re = -10$, $\beta = \infty$ and $De = 0.0$. The outcomes for shear stresses are attained using limiting cases of flow of viscous fluid and compared to those in the study of Abu-Nada and Oztop.³² They are completely in sync.

Discussion of the results

This study numerically described the mass and heat transfer properties of a Casson fluid flowing between two porous discs. The temperature, velocity and concentration profiles' numerical values are displayed. The variation of each parameter revealed a detailed graphical analysis, while the values of the remaining parameters, such as $\beta = 0.5$, $De = 0.2$, $Re = 0.5$, $M = 0.1$, $\text{Pr} = 6.2$,

Table 1. Comparison of the current numerical results for a limiting case of viscous fluid flow with those in the studies of Wehgal and Ashraf¹³ and Mushtaq et al.³

M	$\tilde{f}_1''(-1)$			$\tilde{f}_1''(+1)$		
	Wehgal and Ashraf ¹³	Mushtaq et al. ³	Present	Wehgal and Ashraf ¹³	Mushtaq et al. ³	Present
0.8	2.593 6	2.593 7	2.593600871	2.593 6	2.593 7	2.593600865

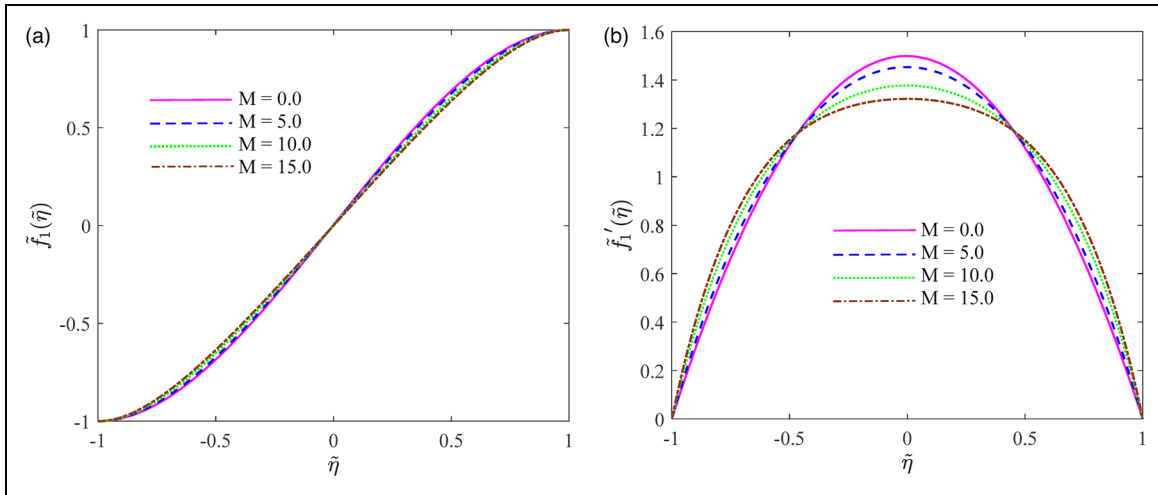


Figure 2. (a) Deviation of $\tilde{f}_1(\tilde{\eta})$ along with M . (b) Deviation of $\tilde{f}_1'(\tilde{\eta})$ along with M .

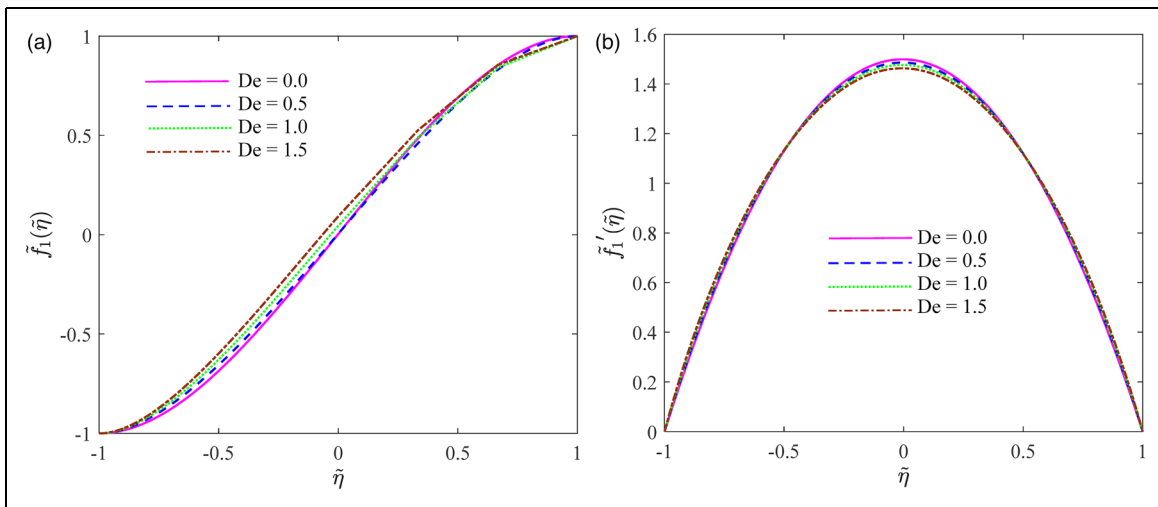


Figure 3. (a) Deviation of $\tilde{f}_1(\tilde{\eta})$ along with De . (b) Deviation of $\tilde{f}_1'(\tilde{\eta})$ along with De .

$\theta_w = 1.2$, $Nt = 0.1$, $Rd = 0.2$, $Nb = 0.1$, $\lambda_1 = 0.2$, $Le = 1.0$ and $\gamma = 0.2$, have remained constant.

Figure 2(a) and (b) shows how the magnetic parameter affects the axial and radial velocity fields. When the values of M are increased, the axial velocity profiles fall at the upper disc while increasing the values of M results in a small increase near the lower disc. A similar pattern can be found in the study of Wehgal and Ashraf.¹³ The radial velocity curves have a parabolic shape. When compared to the magnified magnetic parameter, the profiles show decreasing tendencies in the center plane and increasing tendencies near the upper and lower

discs (see Figure 2). When a magnetic field is applied, the Lorentz force creates a resistive force that obstructs the flow. As a result, around the center plane, the radial profiles are seen to be diminishing.

Figure 3(a) and (b) shows how the Deborah number affects the axial and radial fields. A rise in De generates a rise in axial velocity. As the Deborah number rises, the pumped away from both discs and the central plane's radial velocity profiles decrease. Solid lines (with $De = 0$) illustrate the Casson fluid phenomenon.

Figure 4(a) and (b) depicts the axial and radial velocity profiles as a function of Casson parameter variation.

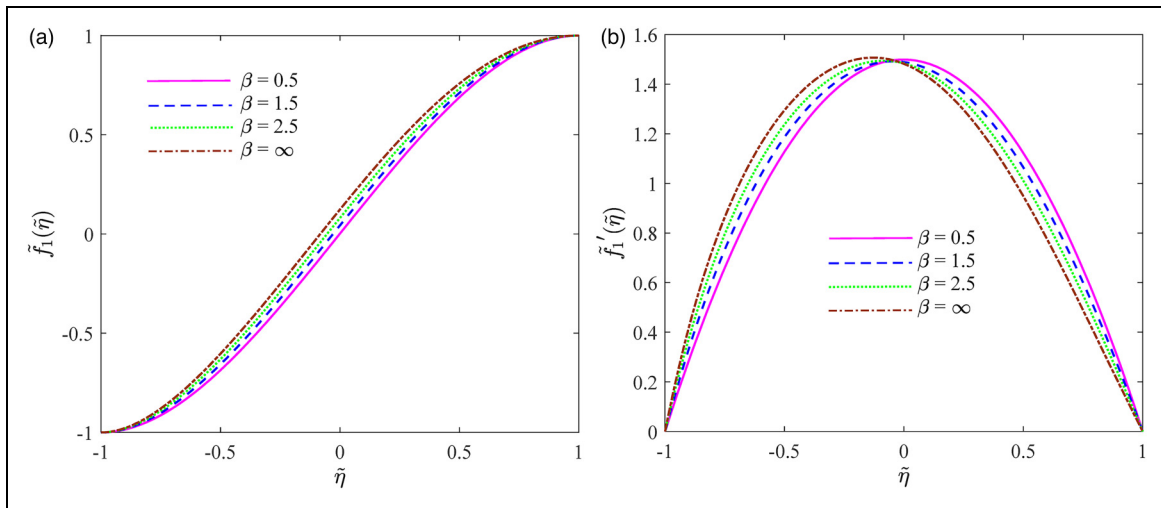


Figure 4. (a) Deviation of $\tilde{f}_1(\tilde{\eta})$ along with β . (b) Deviation of $\tilde{f}_1'(\tilde{\eta})$ along with β .

Because of the increase in β , the axial velocity increases. The Casson parameter has an effect on the declination of the fluid radial velocity in the neighborhood of the central plane. It is because increasing the Casson parameter causes a rise in viscosity, which reduces fluid flow. Dot-dashed lines illustrate the Maxwell liquid situation (as $\beta = \infty$).

Supplementary Figure 1 depicts the thermophoretic parameter Nt archive on the temperature field. The change in Nt builds a significant thermophoretic force that keeps nanoparticles moving in the opposite direction, increasing temperature and boundary layer thickness. These findings are associated with the thermophoresis phenomena, in which heated particles migrate from hotter to colder regions, causing the liquid temperature to rise.

The features of the Brownian motion parameter (Nb) in response to temperature and solutal profiles are shown in Supplementary Figures 2 and 3. Increasing the value of (Nb) enhances the thermal profile and thickness of the thermal boundary layer, as can be shown. However, increasing the solutal profile of the (Nb) nano-Maxwell liquid reduces the thickness of the solutal boundary layer. In terms of physics, intensification in (Nb) refers to an increase in the kinetic energy of nanoparticles in the liquid, which leads to an increase in the rate of heat transfer, the thickness of the boundary layer and the temperature field of Casson–Maxwell nanoliquid. Nanoparticle diffusion in the domain distant from the boundary is also governed by Brownian motion. As a result of raising the Brownian motion parameter, the volume fraction profile of nanoparticles decreases.

Supplementary Figure 4 depicts the behavior of the radiation factor Rd as a function of temperature. The graph showed that the temperature field increased with higher Rd estimates and decreased after the central region. Radiation is the physical process of obtaining energy through fluid molecules. As a result, heat energy is generated in the system, and we see an increase in $\tilde{\theta}_1$ for higher Rd . The temperature variations in thermal

relaxation time are depicted in Supplementary Figure 5. Fluid consumes more heat at the lower disc. However, the surface temperature decreases in the upper disc. Additionally, an increase in the thermal relaxation value (λ_1) implies that more heat is necessary for the heat transfer to the material's neighbor particles (non-conducting phenomena).

Supplementary Figure 6 shows the variation in $\tilde{\theta}_1$ produced by various values of the surface heat parameter θ_w , demonstrating that the temperature distribution grows. Supplementary Figure 7 shows that increasing the values of Le causes the concentration profiles to fall at the upper disc while causing a small increase near the lower disc. Reverse mass diffusivity relationships are achieved, resulting in lower concentration for leading values of Le .

The effect of chemical reaction parameters on the concentration profile is shown in Supplementary Figure 8. When a generative chemical reaction is compared to a destructive chemical reaction, the reduction rate is much higher. By suppressing the concentration of the diffusion species, the chemical reaction reduces fluid concentration.

The numerical outcomes of the Sherwood and Nusselt numbers at the two discs for different physical parameters are discussed in Tables 1 and 2. The Reynolds number, thermophoretic parameter, thermal relaxation time parameter, Prandtl number and Brownian motion parameter reduce the Nusselt number, while the radiation factor, temperature ratio parameter and Lewis number increase the Nusselt number numerical values at the lower disc. The Nusselt number is enlarged at the upper disc by, θ_w, Nt and Nb , while it decreases by λ_1, Pr and Le (Table 1). According to Table 3, the Sherwood number has an increasing tendency for larger values of and a decreasing tendency against the modified. At the lower disc, there are Re, Rd, θ_w, Le and Nb . Changes in the radiation factor, temperature ratio, Lewis number, Brownian motion and chemical reaction parameter decrease the upper disc Sherwood number, while

Table 2. Numerical values of the Nusselt number against physical quantities.

Re	Rd	θ_w	λ_1	Pr	Le	Nt	Nb	Nu_{-1r}	Nu_{+1r}
0.1	0.2	1.2	0.2	6.2	1.0	0.1	0.1	0.235643274	0.657235949
0.3								0.148971567	0.419294354
0.5								0.075645756	0.192874565
0.7								0.024861539	0.039919426
0.5	0.0	1.2	0.2	6.2	1.0	0.1	0.1	0.014508636	0.100347760
	0.3							0.105402601	0.235642095
	0.6							0.174080616	0.328810720
	0.9							0.219260496	0.387707652
0.5	0.2	1.1	0.2	6.2	1.0	0.1	0.1	0.062601950	0.186947863
		1.5						0.118225470	0.215357970
		1.9						0.163324359	0.258357890
		2.3						0.194404034	0.335224636
0.5	0.2	1.2	0.1	6.2	1.0	0.1	0.1	0.098765966	0.242467904
			0.2					0.075645756	0.192874565
			0.3					0.045131898	0.111044000
			0.4					0.009534653	0.000021113
0.5	0.2	1.2	0.2	1.0	1.0	0.1	0.1	0.385427736	0.490068338
				2.0				0.305384563	0.454325340
				3.0				0.234585625	0.392960801
				4.0				0.173765594	0.334473201
0.5	0.2	1.2	0.2	6.2	2.0	0.1	0.1	0.076070165	0.203694586
					3.0			0.076390349	0.201268158
					4.0			0.076583536	0.183977475
					5.0			0.076703351	0.183052316
0.5	0.2	1.2	0.2	6.2	1.0	0.2	0.1	0.058673149	0.277619720
						0.3		0.045853074	0.407114831
						0.4		0.035941601	0.604887583
						0.5		0.027412623	0.902755806
0.5	0.2	1.2	0.2	6.2	1.0	0.1	0.2	0.053183954	0.235990886
							0.3	0.036814924	0.283417703
							0.4	0.025125134	0.334662047
0.5	0.2	1.2	0.2	6.2	1.0	0.1	0.5	0.016929414	0.389205142

changes in the thermophoresis parameter and thermal relaxation parameter increase it (Table 2).

Statistical evaluations

Association metric

To find the association between X and Y , Pearson's coefficient of correlation is the most useful technique in statistics:

$$\left\{ \begin{array}{l} C_{xx} = \sum_{i=1}^n x_i^2 - \frac{1}{n} \left(\sum_{i=1}^n x_i \right)^2, \quad C_{yy} = \sum_{i=1}^n y_i^2 - \frac{1}{n} \left(\sum_{i=1}^n y_i \right)^2, \\ C_{xy} = \sum_{i=1}^n x_i y_i - \frac{1}{n} \sum_{i=1}^n x_i \sum_{i=1}^n y_i, \end{array} \right. \quad (22)$$

$$S_{xy} = \frac{C_{xy}}{\sqrt{C_{xx} \cdot C_{yy}}}, \quad (23)$$

where S_{xy} denotes the correlation between x and y and is always between -1 and $+1$. C_{xx} , C_{yy} and C_{xy} are the variances of x and y , as well as the covariances of x and y ,

respectively. We calculate the correlation between the parameters and variables in Supplementary Table 1 using equation (22). Only between λ_1 and Nu_{+1r} ($S_{xy} = -0.98588898$) is there a reasonable negative linear association in Supplementary Table 1. There are moderately positive linear associations between Re and Nu_{+1r} ($S_{xy} = -0.99540753$) and between λ_1 and Sh_{+1r} ($S_{xy} = 0.992450219$). The remaining parameters and variables have strong positive ($0.70 < S_{xy} < 1$) and negative ($-0.70 < S_{xy} < -1$) correlation.

Statistical significance of correlation

The hypothesis testing procedure is used to determine the statistical significance. To begin, the null (H_0) and alternative (H_A) hypotheses are defined. (H_0) indicates that x and y have no significant linear relationship; (H_A) indicates that x and y have a significant linear relationship. Second, we compute the t -value using the bivariate normality assumption³⁶ $t = S_{xy} \sqrt{n-2} / \sqrt{1-S_{xy}^2}$. Finally, we compute the probability value using the t -value (p -value). Finally, if the p -value is less than the α -level, we accept the alternative hypothesis and determine the

Table 3. Numerical values of the Sherwood number against physical quantities.

Re	Rd	θ_w	λ_1	Le	Nt	Nb	γ	Sh_{-1r}	Sh_{+1r}
0.1	0.2	1.2	0.2	1.0	0.1	0.1	0.2	1.108701113	0.125447360
0.3								0.822546195	0.254991584
0.5								0.616651528	0.311542810
0.7								0.458884556	0.364741174
0.5	0.0	1.2	0.2	1.0	0.1	0.1	0.2	0.617010256	0.369975047
	0.3							0.609359568	0.287606720
	0.6							0.586607233	0.231355181
	0.9							0.569016196	0.193570294
0.5	0.2	1.1	0.2	1.0	0.1	0.1	0.2	0.620733568	0.312170252
		1.5						0.598943617	0.309752013
		1.9						0.574206537	0.306094664
		2.3						0.551210409	0.292255625
0.5	0.2	1.2	0.1	1.0	0.1	0.1	0.2	0.604816473	0.272594704
			0.2					0.616651528	0.311542810
			0.3					0.631710373	0.377172302
			0.4					0.646009515	0.411095585
0.5	0.2	1.2	0.2	2.0	0.1	0.1	0.2	0.487745390	0.171903874
				3.0				0.444225172	0.113430904
				4.0				0.427335120	0.080417433
				5.0				0.419278208	0.062878178
0.5	0.2	1.2	0.2	1.0	0.2	0.1	0.2	0.744405347	0.429878966
					0.3			0.844523289	0.53817095
					0.4			0.920641424	0.624279836
					0.5			0.977175874	0.670839078
0.5	0.2	1.2	0.2	1.0	0.1	0.2	0.2	0.530161243	0.200354911
						0.3		0.501626453	0.162151382
						0.4		0.487699129	0.142102560
						0.5		0.479661401	0.129280863
0.5	0.2	1.2	0.2	1.0	0.2	0.1	-0.2	-0.108350353	0.468174461
							0.1	0.105456059	0.410778743
							0.0	0.293164933	0.368642687
							0.1	0.462040824	0.336607765
0.5	0.2	1.2	0.2	1.0	0.2	0.1	0.2	0.616651528	0.311542810

statistical significance of S_{xy} on (a significance level set at 0.05). If the p -value is greater than the α -level, the null hypothesis is accepted.

Supplementary Table 2 shows the calculated t and p values. The table also shows no significant correlation between (p -value $>$ α) among (Re , Nu_{+1r}), (Re , Sh_{-1r}), (Nb , Sh_{+1r}), (Nb , Sh_{-1r}) and all pairings of λ_1 using the Sherwood and Nusselt numbers at the specified α -level. There are significant linear relationships between the remaining parameters and variables.

Remarks

It investigated the flow of an incompressible Casson nanofluid contained in stationary parallel discs. The energy equation creates a modified version of Fourier's law along with the nonlinear thermal radiation. Additionally, for the associated flow scenario, chemical reaction assumptions for concentration distribution are applied. The resulting ordinary differential equations are solved using an efficient FEM analysis, and the velocity, temperature and concentration profiles are represented with

graphs. For various physical constants, the physical parts of the study are realized. The following noteworthy findings emerged from the current study:

1. At the central plane, the magnetic and Casson parameters reduce the radial curves.
2. The presence of radiation and Brownian motion parameters causes the temperature distribution to rise, whereas the thermal relaxation parameter has the opposite effect.
3. Increases in destructive chemical reactions improve the concentration profile, whereas Brownian motion and generative chemical reactions have the opposite effect.
4. The heat transfer gradient at the lower disc is a growing function of thermal radiation when the temperature ratio is present, and it is a diminishing function when Reynolds number and Brownian motion are present.
5. The local Nusselt number for Brownian motion and thermophoresis factors is increased due to the upper disc, while it is decreased for thermal relaxation time and Prandtl number.

6. When the Reynolds number and Brownian motion are increased, the local mass transport becomes smaller, whereas it accelerates for the lower disc due to thermophoresis.
7. The Sherwood number increased for Reynolds number and thermal relaxation time in the upper disc situation, but it decreased for Lewis number and chemical reaction parameter.
8. λ_1 and Nu_{+1r} have a moderately negative linear relationship. Re and Nu_{+1r} have a moderately positive linear relationship. Because the aforementioned quantities have a moderate linear relationship, randomness can affect one or both of them, causing the weak relationship noticeable.

Acknowledgments

The authors are very grateful to the editor and reviewers for their constructive suggestions.

Declaration of conflicting interests

The author(s) declared no potential conflicts of interest with respect to the research, authorship, and/or publication of this article.

Funding

The author(s) received no financial support for the research, authorship, and/or publication of this article.

ORCID iDs

Kotha Gangadhar  <https://orcid.org/0000-0002-0264-2512>
Konduru Bhanu Lakshmi  <https://orcid.org/0000-0001-8168-4667>

Supplemental material

Supplemental material for this article is available online.

References

1. Mahanthesh B, Gireesha BJ, Shashikumar NS, et al. Marangoni convection in Casson liquid flow due to an infinite disk with exponential space dependent heat source and cross-diffusion effects. *Results Phys* 2018; 9: 78–85.
2. Shehzad SA, Mabood F, Rauf A, et al. Forced convective Maxwell fluid flow through rotating disk under the thermophoretic particles motion. *Int Commun Heat Mass Transf* 2020; 116: 104693.
3. Mushtaq T, Rauf A, Shehzad SA, et al. Numerical and statistical approach for Casson-Maxwell nanofluid flow with Cattaneo-Christov theory. *Appl Math Mech Engl Ed* 2021; 42: 1063–1076.
4. Nazir U, Saleem S, Nawaz M, et al. Three-dimensional heat transfer in nonlinear flow: a FEM computational approach. *J Therm Anal Calorim* 2020; 140: 2519–2528.
5. Obalalu AM, Ajala OA, Akindele AO, et al. Effect of melting heat transfer on electromagnetohydrodynamic non-Newtonian nanofluid flow over a Riga plate with chemical reaction and Arrhenius activation energy. *Eur Phys J Plus* 2021; 136: 891.
6. Lanjwani HB, Chandio MS, Anwar MI, et al. MHD laminar boundary layer flow of radiative Fe-Casson nanofluid: stability analysis of dual solutions. *Chin J Phys* 2022; 76: 172–186.
7. Givi GM and Sangeetha George K. Influence of radiative heat flux in nonlinear convection of quartic order in Casson fluid past a vertical permeable plate with variable suction and Hall current. *Chin J Phys* 2021; 74: 209–225.
8. Mahmud K, Mehmood R, Rana S, et al. Flow of magnetic shear thinning nano fluid under zero mass flux and Hall current. *J Mol Liq* 2022; 352: 118732.
9. Nandeppanavar MM, Kemparaju MC and Raveendra N. Double-diffusive free convective flow of Casson fluid due to a moving vertical plate with non-linear thermal radiation. *World J Eng* 2021; 18: 85–93.
10. Das S, Banu AS and Jana RN. Delineating impacts of non-uniform wall temperature and concentration on time-dependent radiation-convection of Casson fluid under magnetic field and chemical reaction. *World J Eng* 2021; 18: 780–795.
11. Gangadhar K, Venkata Subba Rao M, Manasa Seshakumari P, et al. Entropy generation on convectively heated surface of Casson fluid with viscous dissipation. *Phys Scr* 2020; 95: 115203.
12. Saleem S, Nadeem S, Rashidi MM, et al. An optimal analysis of radiated nanomaterial flow with viscous dissipation and heat source. *Microsyst Technol* 2019; 25: 683–689.
13. Wehgal AR and Ashraf M. MHD asymmetric flow between two porous disks. *Punjab Univ J Math* 2012; 44: 9–21.
14. Turkyilmazoglu M. Flow and heat simultaneously induced by two stretchable rotating disks. *Phys Fluids* 2016; 28: 043601.
15. Ashraf M and Wehgal AR. MHD flow and heat transfer of micropolar fluid between two porous disks. *Appl Math Mech Engl Ed* 2012; 33: 51–64.
16. Reddy NN, Reddy YD, Rao VS, et al. Multiple slip effects on steady MHD flow past a non-isothermal stretching surface in presence of Soret, Dufour with suction/injection. *Int Commun Heat Mass Transf* 2022; 134: 106024.
17. Mahabaleshwar US, Vishalakshi AB and Hatami M. MHD micropolar fluid flow over a stretching/shrinking sheet with dissipation of energy and stress work considering mass transpiration and thermal radiation. *Int Commun Heat Mass Transf* 2022; 133: 105966.
18. Jamshed W, Eid MR, Hussain SM, et al. Physical specifications of MHD mixed convective of Ostwald-de Waele nanofluids in a vented-cavity with inner elliptic cylinder. *Int Commun Heat Mass Transf* 2022; 134: 106038.
19. Blishchik A, Glavinic I, Wondrak T, et al. Effects of electrically conductive walls on turbulent magnetohydrodynamic flow in a continuous casting mold. *Int J Heat Fluid Flow* 2022; 95: 108967.
20. Gireesha BJ, Nagaraja B, Srikantha N, et al. Magnetically propelled Carreau fluid flow over penetrable sensor surface influenced by thermal radiation, Joule heating and heat generation. *Commun Theor Phys* 2022; 74: 025002.
21. Ahmad S, Khan MN, Nadeem S, et al. Impact of Joule heating and multiple slips on a Maxwell nanofluid flow past a slandering surface. *Commun Theor Phys* 2022; 74: 015001.
22. Narasimha Rao NSLV and Gangadhar K. Hall and ion-slip effects on MHD natural convective flow past an unbounded vertical porous channel with thermodiffusion. *Heat Transfer* 2022; 51: 1501–1523.
23. Fourier JBJ. *Théorie Analytique de la Chaleur*. Paris: Didot, 1822.
24. Cattaneo C. Sulla conduzione del calore. *Atti Semin Mat Fis Univ Modena Reggio Emilia* 1948; 3: 83–101.
25. Christov CI. On frame indifferent formulation of the Maxwell-Cattaneo model of finite-speed heat conduction. *Mech Res Commun* 2009; 36: 481–486.

26. Hashim and Khan M. On Cattaneo-Christov heat flux model for Carreau fluid flow over a slendering sheet. *Results Phys* 2017; 7: 310–319.
27. Bai Y, Wang Q and Zhang Y. Unsteady stagnation-point flow of upper-convected Oldroyd-B nanofluid with variable thermal conductivity and relaxation-retardation double-diffusion model. *Int J Numer Methods Heat Amp Fluid Flow* 2021; 31: 3373–3393.
28. Ali M, Sultan F, Khan WA, et al. Characteristics of generalized Fourier's heat flux and homogeneous-heterogeneous reaction in 3D flow of non-Newtonian cross fluid. *Int J Numer Methods Heat Amp Fluid Flow* 2021; 31: 3304–3318.
29. Venkata Ramana K, Gangadhar K, Kannan T, et al. Cattaneo-Christov heat flux theory on transverse MHD Oldroyd-B liquid over nonlinear stretched flow. *J Therm Anal Calorim* 2022; 147: 2749–2759.
30. Choi SUS and Eastman JA. Enhancing thermal conductivity of fluids with nanoparticles. *ASME Publ Fed* 1995; 231: 99–106.
31. Buongiorno J. Convective transport in nanofluids. *ASME J Heat Transf* 2006; 128: 240–250.
32. Abu-Nada E and Oztop HF. Effect of inclination angle on natural convection in enclosure filled with Cu-water nanofluid. *Int J Heat Fluid Flow* 2009; 30: 669–106.
33. López A, Ibáez G, Pantoja J, et al. Entropy generation analysis of MHD nanofluid flow in a porous vertical microchannel with nonlinear thermal radiation, slip flow and convective-radiative boundary conditions. *Int J Heat Mass Transf* 2017; 107: 982–994.
34. Kumar R, Seth GS and Bhattacharyya A. Entropy generation of von Karman's radiative flow with Al_2O_3 and Cu nanoparticles between two coaxial rotating disks: a finite-element analysis. *Eur Phys J Plus* 2019; 134: 597.
35. Gangadhar K, Manasa Seshakumari P, Venkata Subba Rao M, et al. MHD flow analysis of a Williamson nanofluid due to Thomson and Troian slip condition. *Int J Appl Comput Math* 2022; 8: 6.
36. Pearson K. Notes on regression and inheritance in the case of two parents. *Proc R Soc Lond* 1985; 58: 240–242.
37. Salari M, Assari MR, Ghafouri A, et al. Experimental study on forced convection heat transfer of a nanofluid in a heat exchanger filled partially porous material. *J Therm Anal Calorim* 2022; 147: 509–523.
38. Bendaraa A, Charafi MM and Hasnaoui A. Upwind scheme to solve time-periodic temperature effect on convective nanofluid flow in a square cavity. *Eur Phys J Plus* 2022; 137: 224.
39. Roodbari M, Alimoradi H, Shams M, et al. An experimental investigation of microstructure surface roughness on pool boiling characteristics of TiO_2 nanofluid. *J Therm Anal Calorim* 2022; 147: 3283–3298.
40. Olayemi OA, Obalalu AM, Odetunde CB, et al. Heat transfer enhancement of magnetized nanofluid flow due to a stretchable rotating disk with variable thermophysical properties effects. *Eur Phys J Plus* 2022; 137: 393.
41. Zainal NA, Nazar R, Naganthran K, et al. Slip effects on unsteady mixed convection of hybrid nanofluid flow near the stagnation point. *Appl Math Mech Engl Ed* 2022; 43: 547–556.